Dynamics of soot surface growth and agglomeration by enclosed spray combustion of jet fuel

Author(s):
Trivanovic, Una; Pereira Martins, Michael; Benz, Simon; Kelesidis, Georgios A.; Pratsinis, Sotiris E.

Publication date:
2023-06

Permanent link:
https://doi.org/https://doi.org/10.3929/ethz-b-000601640

Originally published in:
Fuel 342, https://doi.org/10.1016/j.fuel.2023.127864

Funding acknowledgement:
- Tailor-made Carbonaceous Nanoparticles by Multiscale Combustion Design ()
- Multifunctional nanoparticles for targeted theranostics ()
- Integrated system for in operando characterization and development of portable breath analyzers ()

Fuel 342 (2023) 127864

Contents lists available at ScienceDirect

Fuel

journal homepage: www.elsevier.com/locate/fuel

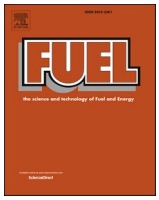

Full Length Article

Dynamics of soot surface growth and agglomeration by enclosed spray combustion of jet fuel

Una Trivanovic, Michael Pereira Martins, Simon Benz, Georgios A. Kelesidis, Sotiris E. Pratsinis *

Particle Technology Laboratory, Institute of Energy & Process Engineering, Department of Mechanical and Process Engineering, ETH Zürich, Sonneggstrasse 3, CH-8092 Zürich, Switzerland

ARTICLE INFO

Keywords:
Soot
Nanostructure
Primary particle size
Aircraft-like soot
Raman spectroscopy

ABSTRACT

Understanding the dynamics of soot formation and growth during combustion of jet fuel is essential for mitigation of aircraft engine emissions. Here, soot formation during enclosed spray combustion of jet fuel is investigated for its capacity to form soot with comparable characteristics to that from aircraft engines. For this, microscopy, scanning mobility particle, X-ray diffraction & Raman spectroscopy measurements and discrete element modeling (DEM) are employed along the flame centerline at various Effective eQuivalence Ratios (EQR). The DEM-derived mobility and primary particle size distribution dynamics are in excellent agreement with those measured at 5–63 cm height above the burner (HAB) for the measured temperature and soot volume fraction. At low EQR (1.46 and 1.59), soot surface growth stops at residence time, t = 4–7 ms, resulting in median soot primary particle diameters, $\bar{d}_p$, of ~ 14 nm. At longer t (high HAB), agglomeration takes over increasing the median mobility diameter from 16 to 88 or 145 nm at EQR of 1.46 or 1.59, respectively, without altering $\bar{d}_p$ and having the disorder over graphitic Raman band ratio, D/G = 0.9 ± 0.01 and a crystallite length, L_c = 1.24 ± 0.02 nm. In contrast, increasing EQR from 1.59 to 1.88, enhances soot surface growth, increases $\bar{d}_p$ up to 23 nm and results in more graphitic soot having D/G = 0.8 ± 0.01 and L_c = 1.47 ± 0.01 nm. Furthermore, the D/G of soot is inversely proportional to its $\bar{d}_p$ that is determined largely by surface growth.

1. Introduction

Aircraft engines are significant sources of ultrafine soot agglomerates [1] that have large inflammatory and cytotoxic responses [2] and contribute to global warming through their direct radiative forcing [3] while they facilitate formation of ice nuclei and contrail cirrus clouds [4]. The mobility diameter, d_m, of such agglomerates determines their transport and lifetime in the atmosphere [5] as well as their deposition in our respiratory system [6]. The primary particle (PP) diameter, d_p, and nanostructure of soot largely determine its oxidative reactions [7] and cytotoxicity [8]. So, understanding the relation between combustion conditions and soot size, composition and morphology is essential to quantify and mitigate the impact of such emissions on climate change and public health.

The size distribution of soot agglomerates from jet fuel combustion in an aircraft engine varies significantly with the applied thrust as summarized recently [9]. The nanostructure of aircraft soot emissions is commonly quantified by the disorder and graphitic bands of their Raman spectrum that is hardly affected by thrust [10]. Monitoring the dynamics of soot nanoparticles during combustion in an aircraft engine is essential to explain the impact of thrust on formation of soot and assist mitigation of its emissions. This can be done by probe or thermophoretic sampling that require though substantial modifications of the engine design [11]. So, aircraft soot emissions have been sampled only at the exhaust of the engine [12].

In this regard, monitoring the dynamics of soot in flame reactors that generate soot with equivalent characteristics to aircraft soot can provide the much needed understanding of soot formation in aircraft engines [13]. The soot d_m and d_p [14] have been measured using scanning mobility particle sizers (SMPS) and microscopy in laminar premixed ethylene [15], propene [16], ethane or acetylene [17] flames at various Effective eQuivalence Ratios (EQRs) [18] that led to similar median $\bar{d}_m$ and $\bar{d}_p$ with those of aircraft soot emissions [19]. However, such premixed flame soot contains large amounts of organic carbon [20] and

* Corresponding author.
E-mail address: sotiris.pratsinis@ptl.mavt.ethz.ch (S.E. Pratsinis).

https://doi.org/10.1016/j.fuel.2023.127864
Received 8 September 2022; Received in revised form 12 February 2023; Accepted 14 February 2023
Available online 3 March 2023

thus is less graphitic than aircraft soot [10]. Furthermore, the light hydrocarbons (e.g. ethylene, propene, ethane, acetylene) used as fuel in the above reactors result in lower soot mass concentrations than those from jet fuel combustion [9] due to limited soot nucleation [21].

Recently, it was shown that enclosed spray combustion of jet fuel produces soot agglomerates at high concentrations with similar morphology, size distribution and organic carbon content with those of aircraft emissions [9]. The high concentrations allowed for analysis of the specific surface area, *SSA*, with N_2 adsorption which is typically not feasible due to the low mass of soot collected from the aircraft exhausts. Here, the dynamics of soot formation and growth are monitored during enclosed spray combustion of jet fuel [9] along the burner centerline. The flame EQR is varied from 1.46 to 1.88 to quantify its impact on the evolution of the soot size distribution and composition by mobility, microscopy and Raman spectroscopy measurements along with discrete element modeling (DEM) simulations. Understanding soot dynamics during enclosed spray combustion of jet fuel can assist the development of robust models to guide the design and operation of aircraft engines with minimal soot emissions.

2. Experimental

Soot was generated by jet A1 fuel ($C_{11.6}H_{22}$ [22]; Birrfeld Airport, Lupfig, Switzerland) enclosed spray combustion [9] using an external-mixing, twin fluid nozzle [23] enclosed in two, 30 cm long stainless steel and quartz tubes (each with a 42 mm inner diameter) in series [24], as shown in Fig. S1 of the Supplementary Information, SI. So, 4.5 mL/min of fuel were dispersed into a fine spray with 0.66–2.0 L/min of O_2 to vary the EQR from 1.46 to 1.88. Given that the true fuel/oxidizer ratio is not known throughout the flame, the "Effective" eQuivalence Ratio (EQR) is calculated accounting for all oxygen sources [9], is:

$$EQR = \frac{\left(\frac{Fuel}{Air}\right)_{Actual}}{\left(\frac{Fuel}{Air}\right)_{Stoichiometric}} \quad (1)$$

The spray was ignited and sustained by a supporting premixed methane/oxygen flame (CH_4 = 1.25 L/min, O_2 = 2.25 L/min). Sheath air was fed through 12 evenly spaced holes surrounding the spray flame at 20 L/min. A torus ring with 12 jet outlets between the two tubes was used to introduce 20 L/min of N_2 in an upward swirled pattern to quench the flame and dilute the exhaust aerosol [25].

The flame temperature, *T*, was measured with the spray present using a 1 mm (nominal) bead diameter, R-type thermocouple (Intertechno-Firag AG) and corrected for radiative heat losses [26]. Without ignition, the spray produces droplets of about 36 μm in diameter at HAB = 6 cm and EQR = 1.46 (Fig. S2). However, these droplets evaporate within a millisecond (HAB ≪ 5 cm) during combustion [27], as *T* increases up to 1603 K at HAB = 5 cm which is much larger than the autoignition *T* = 483 K of jet A1 fuel [28]. Phase-Doppler anemometry and computational fluid dynamics of ethanol combustion in the same burner also indicated that the spray droplets completely evaporate by HAB = 5 cm (i.e. the smallest HAB measured here) [29]. Given that higher temperatures are encountered in enclosed than open burners, fuel droplets evaporate much faster in enclosed ones. For example, in the enclosed flame shown in Fig. 1a of [30] droplets are exposed much longer to high temperatures than in the corresponding open flame (Fig. 1g of [30]) that has a much narrower high temperature zone in its center. So, the probe does not perturb the spray at HAB = 5 cm, as the droplets have already evaporated completely. The thermocouple does not affect the fuel evaporation and subsequent soot aerosol dynamics (Fig. S3) and catalytic effects on the Pt thermocouple surface seem to be negligible. Nonetheless, the mobility and primary particle size distributions were measured here in the absence of a thermocouple. The *T* profile was measured here in a premixed ethylene flame to validate the energy balance used for the radiation correction [26]. The energy balance considers the competition between convection and radiation heat transfer and is used here to extract the flame temperature, *T*, from the bead T_{bead} reading. The excellent agreement between the premixed flame *T* (Fig. S4: symbols & solid line) measured here and that obtained by Öktem et al. [31] (Fig. S4: broken line) indicates that catalytic effects on the Pt thermocouple surface are negligible.

Soot was extracted from the centerline of the flame using a straight sampling probe with an in-flow tube inner diameter of 2.5 mm becoming 5 mm after a 15 mm long entrance [32] at HAB = 5, 10, 15, 20 and 25 cm through five evenly spaced, sealable holes in the bottom stainless steel tube (Fig. S1), as well as at the top of the quartz tube (HAB ~ 63 cm). Since the flame is enclosed by a stainless steel tube, any perturbations induced by the sampling probe cannot be observed. However, measurements at HAB = 63 cm do not seem to be affected by the presence of the thermocouple (Fig. S3). Therefore, the sampling probe does not affect the measurements at the HAB = 5–63 cm investigated here. The sampled aerosol was rapidly diluted and quenched by mixing with N_2, followed by compressed air from a rotating disk diluter and directed to an SMPS, as well as to a glass fiber filter for offline analysis. The sampled aerosol is diluted by a factor of 30 to 45 first using N_2 and then by a factor of 1000 using clean air through a rotating disk diluter, as detailed in [9]. The dilution ratios used here keep the total number concentration of the sampled aerosol at about ~ 10^6 #/cm^3, limiting perturbations of the measured mobility size distribution due to coagulation in the sampling line [32]. The present sampling and dilution system can reduce the temperature of the sampled aerosol down to 264 °C even at the low HAB of 10 cm [32].

The Raman spectra of filter-collected soot nanoparticles were obtained using a 515 nm laser having 50 mW power (Renshaw inVia). The laser was focused with a x20 magnification optical microscope which gives a 2 μm spot size, 10 % laser power was focused on the sample for 120 s and three spectral acquisitions per spot [33]. Raman spectra were obtained and averaged over three positions on the filter surface. The intensities of the disorder (D ~ 1350 cm^{-1}) and graphitic (G ~ 1580 cm^{-1}) bands [33] were obtained after straight line subtraction of the baseline [34]. The ratio of D/G was obtained by simply comparing the intensity (height) of these two peaks. This ratio has been related to the average size of crystalline domains to quantify the degree of soot graphitization based on graphite material studies [35]. The D/G is used here for a comparison of soot graphitization at various HAB and EQR. Soot graphitization was also investigated by X-ray diffraction (XRD) [36]. Briefly, an AXS D8 diffractometer (Bruker) at a scan rate of 0.0197°/s over the range of diffraction angles from 2θ = 10° to 70° was used to obtain the peak angle and full width half maximum (FWHM) of the 002 peak. From this, Bragg's law can be used to quantify the crystallite length, L_c and interlayer distance, d_{002} [37].

Soot collected on the filter was imaged by transmission electron microscopy (TEM, FEI Tecnai F30 FEG). The nanoparticles were dispersed in ethanol and placed in an ultrasonic bath for 15 min to break up large agglomerates [23]. A drop of ethanol solution was then placed on lacey carbon TEM grids with a 200 mesh copper support (LC200-Cu-150, Electron Microscopy Sciences) and allowed to dry. The d_p was measured by manually placing ellipses over the PPs in ImageJ [38] and calculating the area-equivalent diameter. >200 PPs were measured for each HAB and EQR to determine the $\bar{d}_p$. The $\bar{d}_p$ levels off after counting 200 PPs (Fig. S5), consistent with microscopy analysis of soot [39] and TiO_2 [40].

3. Theory

Soot formation by surface growth and agglomeration is investigated by DEM assuming extremely fast soot inception [13] and an initial number/size of soot nuclei [41] attained after complete fuel spray evaporation and combustion. Soot oxidation is not considered as it seems negligible during enclosed spray combustion of jet fuel since the soot volume fraction, f_v, increases by surface growth at small HAB and largely levels off at HAB > 25 cm (Fig. S6). So, oxidation does not reduce soot f_v at the combustion conditions employed here and can be neglected. Coalescence is not

included in the present DEM, as soot nanoparticles with $d_m \geq 2$ nm hardly coalesce due to their large C content [42]. So, necking between soot primary particles occurs by surface growth [41].

The DEM-derived dynamics of nascent [41] and mature [43] soot during surface growth and agglomeration have been detailed and validated in simple laminar premixed [41] and diffusion [43] flames using ethylene [39], propane [44] and 1-decene [43] fuels. In brief, 1000 monodisperse soot particles with an initial diameter of 2 nm and number density of 4.5×10^{16} #/m^3 are randomly distributed in a cubic cell. This initial soot diameter is the smallest identified in laminar premixed ethylene flames [45]. Similarly, the initial soot number density that is used here is the largest one measured in a premixed ethylene flame at 0.55 cm HAB [45]. The temperature, T, and residence time of the cubic cell vary as a function of the Knudsen number, Kn, to follow closely the T and average d_m measurements of enclosed spray combustion of jet fuel (Fig. S7). So, the particle velocities and time scale are rescaled using a Gaussian thermostat [46] to follow the Maxwell-Boltzmann distribution obtained based on the measured T.

The Hydrogen Abstraction Carbon Addition (HACA) mechanism [47] is used to account for soot surface growth as DEM simulates soot formation after inception [38]. The H, H_2 and C_2H_2 concentrations involved in soot surface growth by HACA [47] are included in the present DEM [41]. The maximum computed soot f_v can be varied from 5 to 100 parts per billion (ppb) by increasing the H concentration from 0.36 to 7.5 mmol/m^3 [41]. At constant H concentration, varying the acetylene concentration does not affect the computed f_v, as H abstraction from the soot surface is the rate limiting step of the HACA mechanism [47]. The initial number of hydrogen atoms and acetylene molecules is varied to attain the measured maximum soot volume fraction of about 100 ppb.

During enclosed spray combustion, nanoparticles are formed at a wide range of residence times due to turbulence and recirculation [30]. The present DEM follows the average residence time in the flame. The particle-laden flow is treated as pure gas given the low soot volume fractions, $f_v \leq 100$ ppb, during enclosed spray combustion of jet fuel (Fig. S6). The computed mobility diameter, d_m, is obtained from the projected area, A_{proj}, of the DEM-derived soot agglomerates [48]:

$$d_m = 2 \cdot \sqrt{\frac{A_{proj}}{\pi}} \tag{2}$$

The measured d_m is obtained based on the electrical mobility of the sampled soot nanoparticles [49]. In the free molecular and transition regimes, the d_m obtained using the agglomerate A_{proj} (Eq. (2)) is identical to that measured based on its electrical mobility [48]. The gas mean free path, λ, is defined as [50]:

$$\lambda = \frac{2 \cdot \eta}{p \cdot \sqrt{\frac{8 \cdot MW}{\pi \cdot R \cdot T}}} \tag{3}$$

where MW and η are the molecular weight and viscosity of air, respectively, p is the pressure, R the universal gas constant and T the temperature. The residence time and soot dynamics are derived here by DEM only at EQR = 1.46 and 1.59, as Kn (used here to impose the measured T profile in the simulations) could not be measured as a function of HAB at EQR > 1.59. This is due to the large particle number concentrations limiting probe sampling at HAB < 63 cm.

4. Results and discussion

4.1. Flame temperature

Fig. 1 shows the flame T as a function of HAB during enclosed spray combustion of jet fuel at EQR = 1.46 (triangles), 1.59 (circles), 1.73 (squares) and 1.88 (diamonds), the error bars represent the standard deviation between three separate experiments. The T reaches its maximum at HAB = 5–10 cm. As HAB increases, T decreases almost linearly reaching 900–1220 K at 25 cm, consistent with T profiles in premixed ethylene flames [51]. After N_2 is introduced at HAB = 30 cm, T is further reduced reaching 600–690 K at HAB = 63 cm regardless of EQR. Increasing EQR from 1.46 to 1.88 decreases the maximum T from 1603 to 1300 K due to the reduced combustion efficiency [52] consistent with T measurements in ethanol spray flames [29]. The maximum T here is about 300 K lower than the adiabatic flame T of jet A1 vapor in a premixed combustor at each EQR from all O_2 sources [52].

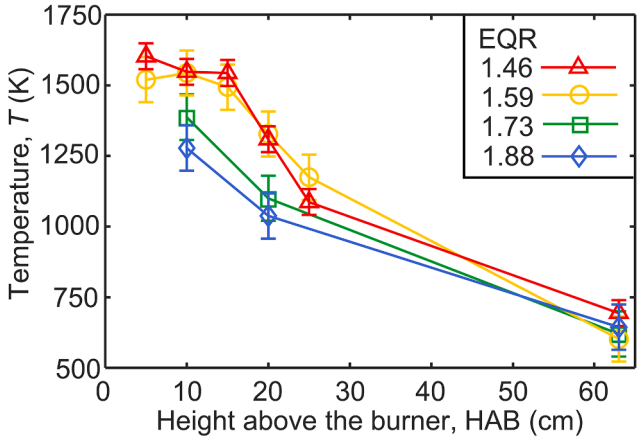

Fig. 1. Flame temperature, T, as a function of HAB during enclosed spray combustion of jet A1 fuel at Effective eQuivalence Ratio, EQR = 1.46 (triangles), 1.59 (circles), 1.73 (squares) & 1.88 (diamonds).

4.2. Soot dynamics along the burner axis

During enclosed spray combustion of jet fuel at EQR = 1.46 (Fig. S8: triangles) and 1.59 (Fig. S8: circles), soot particles experience residence times of about 100 and 400 ms, respectively, at HAB = 30 cm. These residence times are on par with the 60–400 ms obtained by computational fluid dynamics in an identical enclosed burner at a similar HAB [30]. At HAB = 63 cm, these times are 400 and 2500 ms at EQR = 1.46 and 1.59, respectively. Fig. 2 shows the measured (symbols) and DEM-derived (lines) mobility diameter, d_m, distributions of soot at EQR 1.46 and HAB of 5 (d), 15 (c), 25 (b) and 63 cm (a) and the corresponding T (Fig. 1) and representative DEM-derived agglomerate schematics. The shaded area shows the variability of at least 10 SMPS measurements per HAB. For example, increasing HAB from 5 to 25 cm increases the median mobility diameter, $\bar{d}_m$, from 16 to 63 nm, consistent with soot $\bar{d}_m$ dynamics in premixed flames [15]. After introducing N_2 at HAB = 30 cm, the flame T is further reduced (Fig. 1) diluting the aerosol and slowing down coagulation. The mobility size distributions measured here are in excellent agreement with that reported in [9] (Fig. 2a, triangles), further validating the employed experimental methods. So, $\bar{d}_m$ increases only up to 88 nm at HAB = 63 cm. The DEM-derived d_m distributions (lines) span a limited range of d_m because they only account for particles which have experienced an average residence time [41], while in-flame measurements at such turbulent conditions include particles from multiple residence times that are dominated by those around the centerline [53]. At all HABs, the DEM-derived d_m distributions (lines) are in agreement with the measured ones (symbols). Good agreement between DEM simulations and measurements is obtained at all EQR (Fig. S9 for EQR = 1.59) indicating that DEM can follow accurately soot dynamics during enclosed spray combustion of jet fuel given the measured T and soot volume fraction profiles.

Fig. 3 shows the measured (symbols) and DEM-derived (lines) soot $\bar{d}_m$ (circles, solid line) and $\bar{d}_p$ (triangles, broken line), as a function of Knudsen number, Kn, (bottom abscissa) for EQR = 1.46 with exemplary schematics of DEM-calculated agglomerates. The soot Kn was estimated

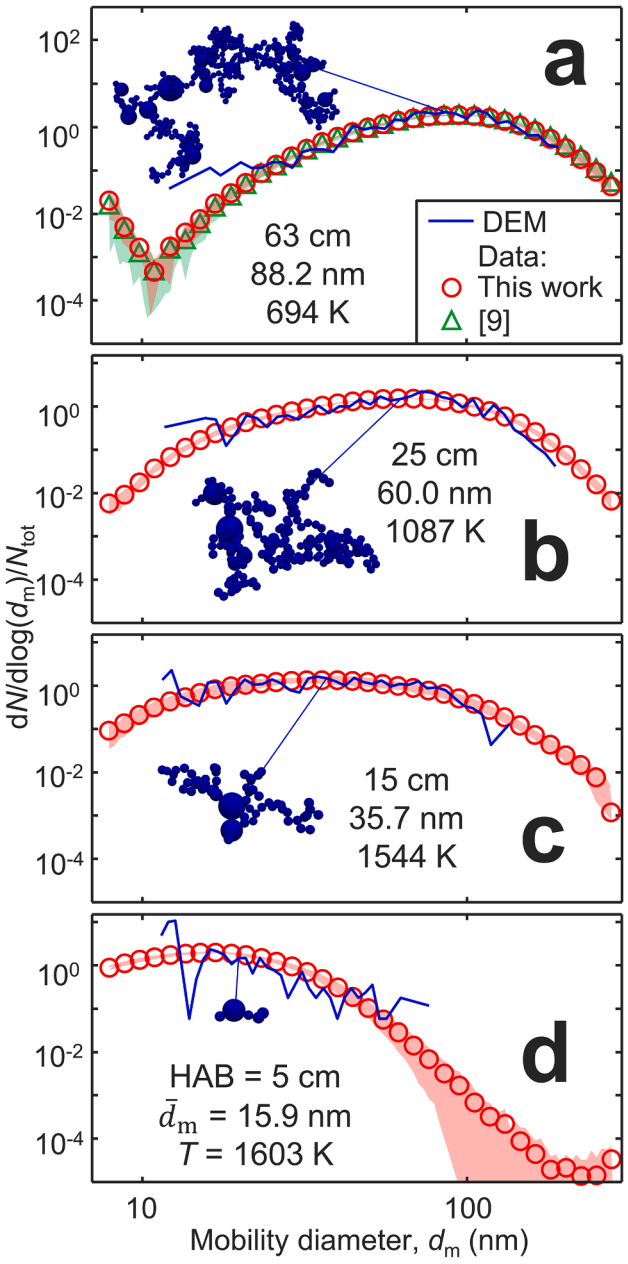

Fig. 2. Mobility diameter, d_m, distributions of soot from enclosed spray combustion of jet fuel at EQR = 1.46 and HAB = 5 (d), 15 (c), 25 (b) and 63 cm (a) from experiments (symbols, shaded area) and DEM simulations (lines) along with representative schemes of the corresponding agglomerate having that $\bar{d}_m$. Circles represent this work, triangles represent data from [9].

from the measured T and $\bar{d}_m$ obtained at various HAB (top abscissa). It was also derived by DEM as a function of t (second top abscissa). The DEM-derived $\bar{d}_m$ and $\bar{d}_p$ are in excellent agreement with the measurements, quantitatively explaining soot dynamics during enclosed combustion of jet fuel. For example, at $t < 12$ ms and HAB < 5 cm, soot grows largely by surface growth, consistent with soot formation in premixed flames [43]. There, soot nanoparticles are rather spherical, having $\bar{d}_m = \bar{d}_p$ that increases up to about 13 nm at t = 7 ms. From then on, agglomeration dominates and increases $\bar{d}_m$ up to 88 nm at HAB = 63 cm, while $\bar{d}_p$ remains rather constant. At higher EQR (i.e. 1.59), both soot number density [54] and coagulation rate increase [51] as agglomeration largely takes over at $t > 4$ ms at this EQR (Fig. S8).

Fig. 4 shows the PP size distributions produced at EQR = 1.46 and

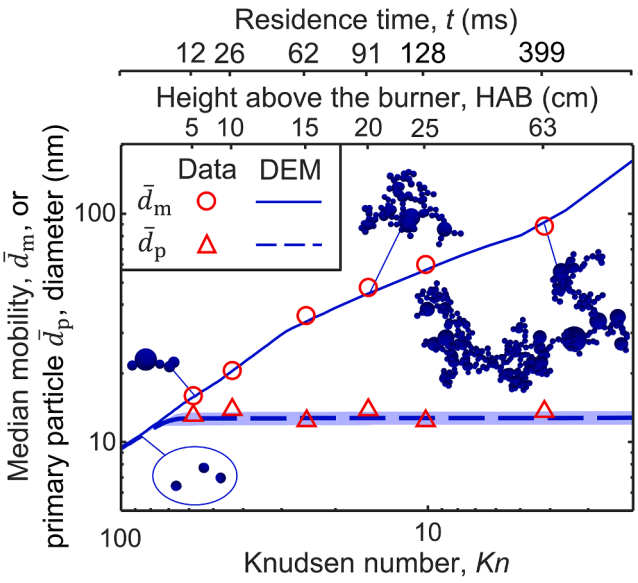

Fig. 3. Median mobility, $\bar{d}_m$, (circles, solid line) and primary particle $\bar{d}_p$, (triangles, broken line) diameters as a function of *Kn* (bottom abscissa), HAB (top abscissa) or residence time, *t*, (second top abscissa) measured (symbols) or derived by DEM (lines) at EQR = 1.46.

measured at HAB = 63 cm (symbols) and derived by DEM at t = 0.8 (dot-broken line), 1.7 (broken line) and 12 (dotted line) that overlays with that of 399 ms or HAB = 63 cm (solid line). The PP size distributions measured at HAB = 5–25 cm (Fig. S10) are practically identical with that measured at HAB = 63 cm (Fig. 4: symbols), consistent with the simulations at t = 12–399 ms. So, the evolution of the PP size distribution during the early stages of soot formation can be elucidated by DEM as it is not possible to measure it there with our instruments. For instance, young soot PPs with $\bar{d}_p$ = 7.4 nm and geometric standard deviation, $\sigma_{g,p}$ = 1.2 are formed by surface growth and aggregation at t = 0.8 ms. As t increases to 1.7 and 12 ms, surface growth dominates, shifting $\bar{d}_p$ to 12.7 nm (Fig. 3, triangles) and $\sigma_{g,p}$ is largely constant, ~ 1.26. Even though coagulation increases agglomerate size (Fig. 3, circles), the soot PP size (d_p) distribution does not change at $t > 7$ ms, as surface growth has levelled off [41]. The DEM-derived PP size distributions obtained at t = 12 and 399 ms overlap and are in agreement with the measured ones. This further validates the present DEM simulations and indicates that surface growth stops at short residence times ($t < 7$

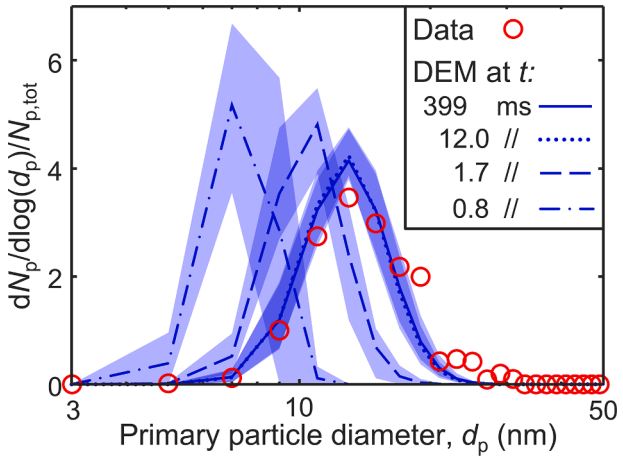

Fig. 4. The PP distributions of soot made at EQR = 1.46 and measured at HAB = 63 cm (symbols) or derived by DEM at t = 0.8 (dot-broken line), 1.7 (broken line), 12 (dotted line) and 399 ms (solid line).

ms) during enclosed combustion of jet fuel.

Fig. 5 shows the Raman spectra along with the ratio of the disorder (D ~ 1350 cm^{-1}) over the graphitic (G ~ 1580 cm^{-1}) band measured at HAB = 5 (double dot-broken line), 10 (dot-broken line), 25 (broken line) and 63 cm (solid line) from soot made at EQR = 1.46 that are quite similar to those made at EQR = 1.59 (Fig. S11). More graphitic soot nanoparticles having D/G = 0.85 ± 0.01 are formed at HAB = 5 cm and T = 1600 K (Fig. 1). As HAB increases from 5 to 10 cm, T decreases (Fig. 1) and D/G increases up to 0.88 ± 0.01.

The Raman spectra dynamics of soot produced at EQR = 1.59 are shown in Fig. S11. Based on the uncertainty error bars, the increase of D/G from 0.85 to 0.9 is not within the experimental noise. This increase is similar to that of D/G of premixed flame soot that had been attributed to increasing soot maturity [55]. X-ray photoelectron spectroscopy suggests that this increase of soot D/G can be attributed to reactions at the soot surface that increase the sp^3-hybridized carbon content [56]. Above HAB = 10 cm, D/G asymptotically reaches 0.87–0.89. Similar asymptotic D/G are obtained at EQR = 1.59 (Fig. S11).

This is attributed to coagulation at low T < 1500 K (Fig. 1) that does not affect soot nanostructure [57] as limited oxidation is expected to take place in the enclosed flame environment especially after injection of 20 L/min of N_2 at 30 cm HAB. The Raman spectra of soot generated here at EQR ≤ 1.59 and HAB = 63 cm are in agreement with that of aircraft soot (Fig. 5, dotted line) [10]. This indicates that the nanostructure of soot produced here at low EQR is similar to that of aircraft emissions.

4.3. Impact of EQR on soot PP size distribution and nanostructure

Fig. 6a shows the d_p distributions along with the median $\bar{d}_p$ and $\sigma_{g,p}$ of soot produced by enclosed spray combustion of jet fuel at EQR = 1.46–1.88 at HAB = 63 cm. The d_p distribution is hardly affected at EQR of 1.46 and 1.59, resulting in a $\bar{d}_p$ of about 14 nm, consistent with our previous work [9]. Increasing EQR to 1.73 or 1.88 though, increases $\bar{d}_p$ to 20 or 23 nm, respectively, consistent with measurements in rich premixed [39] and diffusion flames [58]. This can be attributed to enhanced surface growth [43] or prolonged high temperature residence times [41] at high EQR.

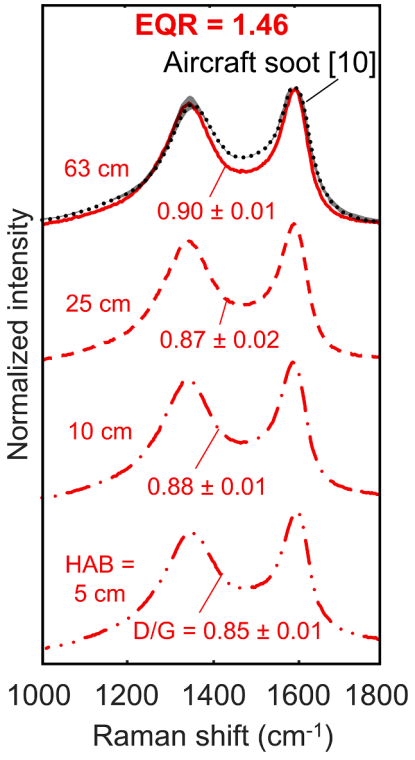

Fig. 5. Normalized intensity as a function of Raman shift measured from soot produced by enclosed combustion of jet fuel spray at EQR = 1.46 and HAB = 5 cm (double dot-broken line), 10 (dot-broken line), 25 (broken line) and 63 cm (solid line) in comparison to that of aircraft soot (dotted line [10]).

Fig. 6b shows the Raman spectra along with the D/G of soot produced at EQR = 1.46–1.88 at HAB = 63 cm. The Raman spectrum of soot made at EQR = 1.59 is almost identical to that obtained at EQR = 1.46 and the same HAB (Fig. 5) having D/G = 0.90 ± 0.01. Further increasing EQR to 1.73 and 1.88 decreases D/G to 0.82 ± 0.01 and 0.80 ± 0.01, respectively. This indicates that soot nanoparticles produced at EQR > 1.59 are more graphitic than those made at lower EQR. This is despite the low T at EQR > 1.59 (Fig. 1) which results in less graphitic nanoparticles in premixed flame reactors [57]. The valley between the D and G peaks, as well as their full width at half maximum increases with increasing EQR. This is due to the secondary D2, D3 and D4 Raman bands that are attributed to surface graphene defects, amorphous carbon, polyenes and/or ionic impurities [59]. The width and intensity of these bands increase with increasing organic to total carbon (OC/TC) mass ratio and thus could indicate the adsorption of disordered polyaromatic hydrocarbons on soot [55]. The organic to total carbon (OC/TC) mass ratio was also measured for soot from enclosed spray combustion of jet fuel at EQR = 1.46–1.88 and HAB = 63 cm, as described in [9] (Fig. S12). Increasing EQR from 1.46 to 1.59 decreases the OC/TC of soot from 17.6 to 10.9 %, consistent with past OC/TC measurements of soot made at identical conditions [9]. However, further increasing EQR to 1.88 increases OC/TC up to 14.4 % corroborating such Raman data of premixed flame soot [55].

Fig. 7 presents the soot D/G as a function of its $\bar{d}_p$ at EQR = 1.46–1.88, with selected TEM images of soot. Increasing EQR from 1.46 to 1.88 increases soot $\bar{d}_p$ from 14 to 23 nm while the soot D/G decreases from 0.9 to 0.8. This D/G drop with increasing $\bar{d}_p$ is in excellent agreement with measurements in turbulent diffusion flames (D/G from 11 to 5 for $\bar{d}_p$ increasing from 15 to 25 nm using a 785 nm laser for Raman) [60]. Aerodynamically classifying soot from an inverted ethylene diffusion flame similarly showed a correlation between impactor stage (i.e. aerodynamic diameter, d_a) and the D/G ratio from a 785 nm laser where D/G dropped from 13.5 at stage 4 (d_a = 22–38 nm) to 8.5 at stage 10 (d_a = 560–950 nm) [34]. So, while exposure to high temperatures at relatively long residence times has been shown to graphitize soot [61], $\bar{d}_p$ increases with increasing graphitic content of soot formed by diffusion and spray flames where the high-temperature residence time is short.

To further verify this, the nanostructure of soot from enclosed spray combustion of jet fuel was analyzed with high resolution transmission electron microscopy (HRTEM; Fig. S13). Such images reveal that soot primary particles formed at EQR = 1.46 are rather amorphous and contain polyaromatic hydrocarbons (PAHs) arranged in small crystallites. As EQR increases, soot nanostructure becomes more ordered, and the length of their crystallites increases. This corroborates the Raman spectra obtained here and indicates that increasing EQR results in larger soot primary particles with higher graphitic content. In this regard, Fig. 8 shows the mean interlayer distance, d_{002} (circles), and crystallite length, L_c (triangles), as a function of median d_p of soot produced by enclosed spray combustion at EQR = 1.46–1.88 obtained from XRD patterns as described in [36]. As EQR increases and soot primary particles become larger by surface growth, d_{002} decreases and L_c increases. This further confirms that soot primary particles become more graphitic at increasing EQR and d_p. This can be attributed to enhanced surface growth through the HACA mechanism [47] that is required to produce large, graphitic soot nanoparticles [62] obtained here at HAB = 63 cm. This is also consistent with measurements [54] and simulations [63] in premixed flames showing that increasing EQR increases the soot d_m, decreases its optical band gap and thus enhances its graphitic content.

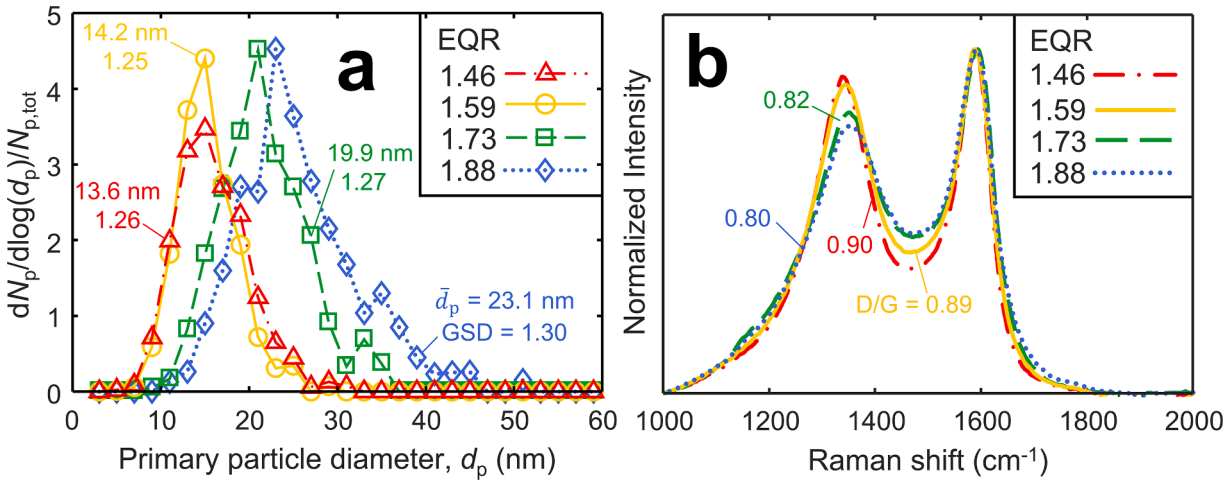

Fig. 6. Soot d_p distributions (a) and Raman spectra (b) obtained from enclosed spray combustion of jet fuel at EQR = 1.46 (triangles, dot-broken line), 1.59 (circles, solid line), 1.73 (squares, broken line) and 1.88 (diamonds, dotted line) at HAB = 63 cm.

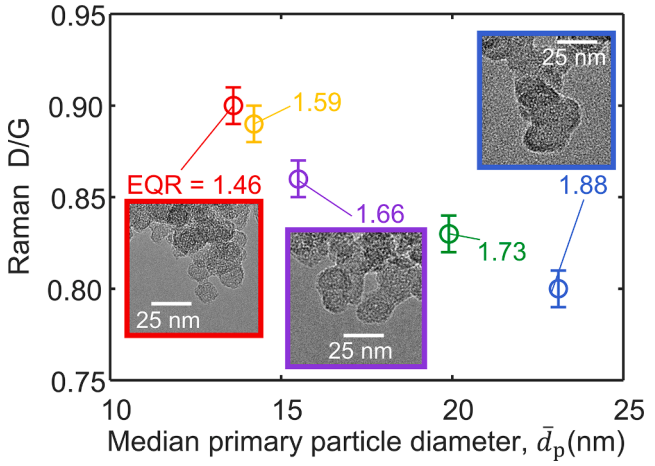

Fig. 7. Soot D/G ratio as a function of its median PP diameter, $\bar{d}_p$, measured here by enclosed spray combustion of jet fuel at EQR = 1.46 – 1.88 at HAB = 63 cm, with TEM images of soot at EQR of 1.46, 1.66 and 1.88.

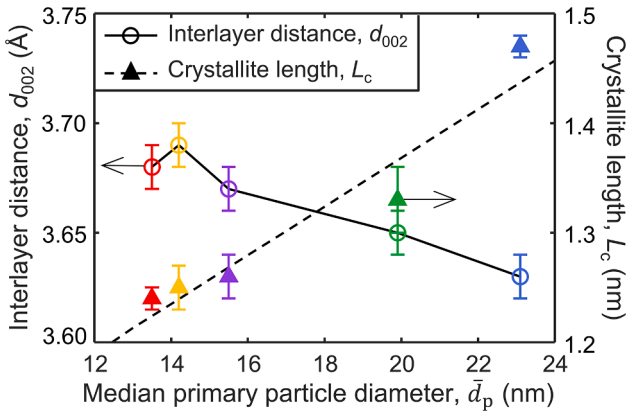

Fig. 8. Mean interlayer distance, d_{002} (circles) and crystallite length, L_c (triangles) as a function of median d_p of soot produced by enclosed spray combustion of jet fuel at EQR = 1.46 – 1.88.

5. Conclusions

The dynamics of soot formed during enclosed spray combustion of jet A1 fuel [9] were investigated numerically and experimentally at HAB = 5–63 cm and EQR = 1.46–1.88. The soot mobility (Fig. 2), primary particle (Fig. 3) size distributions and nanostructure (Fig. 5) measured here as a function of height above the burner (HAB) elucidate in detail the dynamics of soot formation and growth during enclosed spray combustion of jet fuel. These data are explained quantitatively by a discrete element model (DEM) for surface growth and agglomeration [41] that is used to describe such soot aerosol dynamics in spray flames for the first time to the best of our knowledge. The d_m and d_p distributions derived from DEM are in excellent agreement with experimental measurements at all conditions for the measured temperature and soot volume fraction. This shows that, despite the simplified precursor chemistry, flame flow field and average time scale used here, these assumptions capture the essence of the dynamics of the measured soot particle characteristics even though the actual process is far more complex to describe it in detail. At HAB > 5 cm, the $\bar{d}_p$ does not increase as surface growth is limited at EQR = 1.46 or 1.59 ending after t = 7 and 4 ms, respectively, corresponding to HAB < 5 cm, as elucidated by DEM. At these short t, $\bar{d}_p$ = 14 nm and does not grow from HAB = 5 to 63 cm while $\bar{d}_m$ increases by agglomeration to 88 or 145 nm at EQR = 1.46 or 1.59, respectively. At low HAB, the soot nanostructure is slightly more graphitic and becomes more disordered after the maximum temperature is attained at HAB = 5–10 cm for all EQR. At HAB = 63 cm and EQR ≤ 1.59, the soot nanostructure is rather disordered with D/G = 0.9 ± 0.01. As the EQR increases from 1.59 to 1.88, the $\bar{d}_p$ increases to 23 nm through enhanced surface growth and becomes more graphitic having D/G = 0.8 ± 0.01 despite the lower flame temperatures with increasing EQR. This is consistent with observations in turbulent diffusion flames [60]. Thus, the D/G of soot is inversely proportional to its $\bar{d}_p$ that is determined largely by surface growth.

CRediT authorship contribution statement

Una Trivanovic: Conceptualization, Methodology, Validation, Formal analysis, Investigation, Data curation, Writing – original draft, Visualization, Funding acquisition. **Michael Pereira Martins:** Validation, Formal analysis, Investigation, Writing – review & editing. **Simon Benz:** Software, Writing – review & editing, Visualization. **Georgios A. Kelesidis:** Methodology, Writing – review & editing, Supervision, Software. **Sotiris E. Pratsinis:** Conceptualization, Resources, Writing – review & editing, Supervision, Project administration, Funding

acquisition.

Declaration of Competing Interest

The authors declare that they have no known competing financial interests or personal relationships that could have appeared to influence the work reported in this paper.

Data availability

Data will be made available on request.

Acknowledgments

We gratefully acknowledge Dr. F. Krumeich for the TEM imaging and stimulating discussions with Dr. K. Wegner. This research was funded by the Particle Technology Laboratory, ETH Zurich, and in part by Swiss National Science Foundation (200020_182668, 250320_163243 and 206021_170729) and the Natural Sciences and Engineering Research Council of Canada (NSERC CGSD3-547016-2020).

Appendix A. Supplementary data

Supplementary data to this article can be found online at https://doi.org/10.1016/j.fuel.2023.127864.

References

[1] Westerdahl D, Fruin SA, Fine PL, Sioutas C. The Los Angeles International Airport as a source of ultrafine particles and other pollutants to nearby communities. Atmos Environ 2008;42:3143–55. https://doi.org/10.1016/j.atmosenv.2007.09.006.
[2] Cassee FR, Héroux ME, Gerlofs-Nijland ME, Kelly FJ. Particulate matter beyond mass: recent health evidence on the role of fractions, chemical constituents and sources of emission. Inhal Toxicol 2013;25:802–12. https://doi.org/10.3109/08958378.2013.850127.
[3] Kelesidis GA, Neubauer D, Fan LS, Lohmann U, Pratsinis SE. Enhanced light absorption and radiative forcing by black carbon agglomerates. Environ Sci Technol 2022;56:8610–8. https://doi.org/10.1021/acs.est.2c00428.
[4] Kärcher B. Formation and radiative forcing of contrail cirrus. Nat Commun 2018;9:1824. https://doi.org/10.1038/s41467-018-04068-0.
[5] Bond TC, Doherty SJ, Fahey DW, Forster PM, Berntsen T, DeAngelo BJ, et al. Bounding the role of black carbon in the climate system: a scientific assessment. J Geophys Res Atmos 2013;118:5380–552. https://doi.org/10.1002/jgrd.50171.
[6] Rissler J, Swietlicki E, Bengtsson A, Boman C, Pagels J, Sandström T, et al. Experimental determination of deposition of diesel exhaust particles in the human respiratory tract. J Aerosol Sci 2012;48:18–33. https://doi.org/10.1016/j.jaerosci.2012.01.005.
[7] Hagen FP, Kretzler D, Häber T, Bockhorn H, Suntz R, Trimis D. Carbon nanostructure and reactivity of soot particles from non-intrusive methods based on UV-VIS spectroscopy and time-resolved laser-induced incandescence. Carbon 2021;182:634–54. https://doi.org/10.1016/j.carbon.2021.06.006.
[8] Schmid O, Stoeger T. Surface area is the biologically most effective dose metric for acute nanoparticle toxicity in the lung. J Aerosol Sci 2016;99:133–43. https://doi.org/10.1016/j.jaerosci.2015.12.006.
[9] Trivanovic U, Kelesidis GA, Pratsinis SE. High-throughput generation of aircraft-like soot. Aerosol Sci Technol 2022;56:732–43. https://doi.org/10.1080/02786826.2022.2070055.
[10] Parent P, Laffon C, Marhaba I, Ferry D, Regier TZ, Ortega IK, et al. Nanoscale characterization of aircraft soot: a high-resolution transmission electron microscopy, Raman spectroscopy, X-ray photoelectron and near-edge X-ray absorption spectroscopy study. Carbon 2016;101:86–100. https://doi.org/10.1016/j.carbon.2016.01.040.
[11] Zhang R, Kook S. Structural evolution of soot particles during diesel combustion in a single-cylinder light-duty engine. Combust Flame 2015;162:2720–8. https://doi.org/10.1016/j.combustflame.2015.04.008.
[12] Saffaripour M, Thomson KA, Smallwood GJ, Lobo P. A review on the morphological properties of non-volatile particulate matter emissions from aircraft turbine engines. J Aerosol Sci 2020;139:105467. https://doi.org/10.1016/j.jaerosci.2019.105467.
[13] Wang H. Formation of nascent soot and other condensed-phase materials in flames. Proc Combust Inst 2011;33:41–67. https://doi.org/10.1016/j.proci.2010.09.009.
[14] Bladh H, Johnsson J, Olofsson NE, Bohlin A, Bengtsson PE. Optical soot characterization using two-color laser-induced incandescence (2C-LII) in the soot growth region of a premixed flat flame. Proc Combust Inst 2011;33:641–8. https://doi.org/10.1016/j.proci.2010.06.166.
[15] Zhao B, Yang Z, Johnston MV, Wang H, Wexler AS, Balthasar M, et al. Measurement and numerical simulation of soot particle size distribution functions in a laminar premixed ethylene-oxygen-argon flame. Combust Flame 2003;133:173–88. https://doi.org/10.1016/S0010-2180(02)00574-6.
[16] Lin H, Gu C, Camacho J, Lin B, Shao C, Li R, et al. Mobility size distributions of soot in premixed propene flames. Combust Flame 2016;172:365–73. https://doi.org/10.1016/j.combustflame.2016.07.002.
[17] Mei J, Wang M, Hou D, Tang Q, You X. Comparative study on nascent soot formation characteristics in laminar premixed acetylene, ethylene, and ethane flames. Energy Fuel 2018;32:11683–93. https://doi.org/10.1021/acs.energyfuels.8b02852.
[18] Maricq MM, Harris SJ, Szente JJ. Soot size distributions in rich premixed ethylene flames. Combust Flame 2003;132:328–42. https://doi.org/10.1016/S0010-2180(02)00502-3.
[19] Ess MN, Vasilatou K. Characterization of a new miniCAST with diffusion flame and premixed flame options: generation of particles with high EC content in the size range 30 nm to 200 nm. Aerosol Sci Technol 2019;53:29–44. https://doi.org/10.1080/02786826.2018.1536818.
[20] Maricq MM. Examining the relationship between black carbon and soot in flames and engine exhaust. Aerosol Sci Technol 2014;48:620–9. https://doi.org/10.1080/02786826.2014.904961.
[21] Saggese C, Singh AV, Xue X, Chu C, Kholghy MR, Zhang T, et al. The distillation curve and sooting propensity of a typical jet fuel. Fuel 2019;235:350–62. https://doi.org/10.1016/j.fuel.2018.07.099.
[22] Dagaut P, Cathonnet M. The ignition, oxidation, and combustion of kerosene: a review of experimental and kinetic modeling. Prog Energy Combust Sci 2006;32:48–92. https://doi.org/10.1016/j.pecs.2005.10.003.
[23] Mädler L, Kammler HK, Mueller R, Pratsinis SE. Controlled synthesis of nanostructured particles by flame spray pyrolysis. J Aerosol Sci 2002;33:369–89. https://doi.org/10.1016/S0021-8502(01)00159-8.
[24] Teleki A, Heine MC, Krumeich F, Akhtar MK, Pratsinis SE. In situ coating of flame-made TiO_2 particles with nanothin SiO_2 films. Langmuir 2008;24:12553–8. https://doi.org/10.1021/la801630z.
[25] Teleki A, Buesser B, Heine MC, Krumeich F, Akhtar MK, Pratsinis SE. Role of gas – aerosol mixing during in situ coating of flame-made titania particles. Ind Eng Chem Res 2009;48:85–92. https://doi.org/10.1021/ie800226d.
[26] C.R. Shaddix A New Method To Compute the Radiant Correction of Bare-Wire Thermocouples in: 33rd ASME Natl. Heat Transf. Conf. Mediterr. Combust 2017 Symp., Naples, Italy.
[27] Kitano T, Nishio J, Kurose R, Komori S. Evaporation and combustion of multicomponent fuel droplets. Fuel 2014;136:219–25. https://doi.org/10.1016/j.fuel.2014.07.045.
[28] Glassman I, Yetter RA. Combustion. Academic Press; 2007.
[29] Gröhn AJ, Pratsinis SE, Wegner K. Fluid-particle dynamics during combustion spray aerosol synthesis of ZrO_2. Chem Eng J 2012;191:491–502. https://doi.org/10.1016/j.cej.2012.02.093.
[30] Waser O, Brenner O, Groehn AJ, Pratsinis SE. Process design for size-controlled flame spray synthesis of $Li_4Ti_5O_{12}$ and electrochemical performance. Chem Process Eng 2017;38:51–66. https://doi.org/10.1515/cpe-2017-0005.
[31] Öktem B, Tolocka MP, Zhao B, Wang H, Johnston MV. Chemical species associated with the early stage of soot growth in a laminar premixed ethylene – oxygen – argon flame. Combust Flame 2005;142:364–73. https://doi.org/10.1016/j.combustflame.2005.03.016.
[32] Goudeli E, Gröhn AJ, Pratsinis SE. Sampling and dilution of nanoparticles at high temperature. Aerosol Sci Technol 2016;50:591–604. https://doi.org/10.1080/02786826.2016.1168922.
[33] Sadezky A, Muckenhuber H, Grothe H, Niessner R, Pöschl U. Raman microspectroscopy of soot and related carbonaceous materials: Spectral analysis and structural information. Carbon 2005;43:1731–42. https://doi.org/10.1016/J.CARBON.2005.02.018.
[34] Baldelli A, Rogak SN. Morphology and raman spectra of aerodynamically-classified soot samples. Atmos Meas Tech Discuss 2019;12:4339–46. https://doi.org/10.5194/amt-2019-86.
[35] Tuinstra F, Koenig J. Raman spectrum of graphite. J Chem Phys 1970;53:1126–30. https://doi.org/10.1063/1.1674108.
[36] Kelesidis GA, Rossi N, Pratsinis SE. Porosity and crystallinity dynamics of carbon black during internal and surface oxidation. Carbon 2022;197:334–40. https://doi.org/10.1016/j.carbon.2022.06.020.
[37] Iwashita N, Park CR, Fujimoto H, Shiraishi M, Inagaki M. Specification for a standard procedure of X-ray diffraction measurements on carbon materials. Carbon 2004;42:701–14. https://doi.org/10.1016/j.carbon.2004.02.008.
[38] Schneider CA, Rasband WS, Eliceiri KW. NIH Image to ImageJ: 25 years of image analysis. Nat Methods 2012;9:671–5. https://doi.org/10.1038/nmeth.2089.
[39] Kelesidis GA, Kholghy MR, Zuercher J, Robertz J, Allemann M, Duric A, et al. Light scattering from nanoparticle agglomerates. Powder Technol 2020;365:52–9. https://doi.org/10.1016/j.powtec.2019.02.003.
[40] Tsantilis S, Kammler HK, Pratsinis SE. Population balance modeling of flame synthesis of titania nanoparticles. Chem Eng Sci 2002;57:2139–56. https://doi.org/10.1016/S0009-2509(02)00107-0.
[41] Kelesidis GA, Goudeli E, Pratsinis SE. Flame synthesis of functional nanostructured materials and devices: Surface growth and aggregation. Proc Combust Inst 2017;36:29–50. https://doi.org/10.1016/j.proci.2016.08.078.
[42] Mitchell P, Frenklach M. Particle aggregation with simultaneous surface growth. Phys Rev E 2003;67:061407. https://doi.org/10.1103/PhysRevE.67.061407.

[43] Kelesidis GA, Goudeli E, Pratsinis SE. Morphology and mobility diameter of carbonaceous aerosols during agglomeration and surface growth. Carbon 2017; 121:527–35. https://doi.org/10.1016/j.carbon.2017.06.004.
[44] Kelesidis GA, Goudeli E. Self-preserving size distribution and collision frequency of flame-made nanoparticles in the transition regime. Proc Combust Inst 2021;38: 1233–40. https://doi.org/10.1016/j.proci.2020.07.147.
[45] Camacho J, Liu C, Gu C, Lin H, Huang Z, Tang Q, et al. Mobility size and mass of nascent soot particles in a benchmark premixed ethylene flame. Combust Flame 2015;162:3810–22. https://doi.org/10.1016/j.combustflame.2015.07.018.
[46] Woodcock LV. Isothermal molecular dynamics calculations for liquid salts. Chem Phys Lett 1971;10:257–61. https://doi.org/10.1016/0009-2614(71)80281-6.
[47] Appel J, Bockhorn H, Frenklach M. Kinetic modeling of soot formation with detailed chemistry and physics: laminar premixed flames of C2 hydrocarbons. Combust Flame 2000;121:122–36. https://doi.org/10.1016/S0010-2180(99)00135-2.
[48] Rogak SN, Flagan RC, Nguyen HV. The mobility and structure of aerosol agglomerates. Aerosol Sci Technol 1993;18:25–47. https://doi.org/10.1080/02786829308959582.
[49] Hinds WC. Aerosol technology: properties, behavior, and measurement of air borne particles. second ed. Hoboken, New Jersey: John Wiley & Sons; 1999.
[50] Friedlander SK. Smoke, dust and haze: fundamentals of aerosol dynamics. New York: Oxford University Press; 2000.
[51] Ciajolo A, D'Anna A, Barbella R, Tregrossi A, Violi A. The effect of temperature on soot inception in premixed ethylene flames. Symp Combust 1996;26:2327–33. https://doi.org/10.1016/S0082-0784(96)80061-0.
[52] Gülder ÖL. Flame temperature estimation of conventional and future jet fuels. J Eng Gas Turbines Power 1986;108:376–80. https://doi.org/10.1115/1.3239914.
[53] Chowdhury S, Boyette WR, Roberts WL. Time-averaged probability density functions of soot nanoparticles along the centerline of a piloted turbulent diffusion flame using a scanning mobility particle sizer. J Aerosol Sci 2017;106:56–67. https://doi.org/10.1016/j.jaerosci.2016.10.012.
[54] Liu C, Singh AV, Saggese C, Tang Q, Chen D, Wan K, et al. Flame-formed carbon nanoparticles exhibit quantum dot behaviors. Proc Natl Acad Sci 2019;116: 12692–7. https://doi.org/10.1073/pnas.1900205116.
[55] Bocchicchio S, Commodo M, Sgro LA, Chiari M, D'Anna A, Minutolo P. Thermo-optical-transmission OC/EC and Raman spectroscopy analyses of flame-generated carbonaceous nanoparticles. Fuel 2022;310:122308. https://doi.org/10.1016/j.fuel.2021.122308.
[56] Commodo M, D'Anna A, De Falco G, Larciprete R, Minutolo P. Illuminating the earliest stages of the soot formation by photoemission and Raman spectroscopy. Combust Flame 2017;181:188–97. https://doi.org/10.1016/j.combustflame.2017.03.020.
[57] Dasappa S, Camacho J. Evolution in size and structural order for incipient soot formed at flame temperatures greater than 2100 K. Fuel 2021;291:120196. https://doi.org/10.1016/j.fuel.2021.120196.
[58] Ghazi R, Tjong H, Soewono A, Rogak SN, Olfert JS. Mass, mobility, volatility, and morphology of soot particles generated by a mckenna and inverted burner. Aerosol Sci Technol 2013;47:395–405. https://doi.org/10.1080/02786826.2012.755259.
[59] Bonpua J, Yagües Y, Aleshin A, Dasappa S, Camacho J. Flame temperature effect on sp2 bonds on nascent carbon nanoparticles formed in premixed flames (Tf, max 2100 K): a Raman spectroscopy and particle mobility sizing study. Proc Combust Inst 2019;37:943–51. https://doi.org/10.1016/j.proci.2018.06.124.
[60] Trivanovic U, Sipkens TA, Kazemimanesh M, Baldelli A, Jefferson AM, Conrad BM, et al. Morphology and size of soot from gas flares as a function of fuel and water addition. Fuel 2020;279:118478. https://doi.org/10.1016/j.fuel.2020.118478.
[61] Vander Wal RL, Tomasek AJ, Pamphlet MI, Taylor CD, Thompson WK. Analysis of HRTEM images for carbon nanostructure quantification. J Nanoparticle Res 2004; 6:555–68. https://doi.org/10.1007/s11051-004-3724-6.
[62] Hayashida K, Nagaoka S, Ishitani H. Growth and oxidation of graphitic crystallites in soot particles within a laminar diffusion flame. Fuel 2014;128:148–54. https://doi.org/10.1016/j.fuel.2014.03.008.
[63] Kelesidis GA, Pratsinis SE. Soot light absorption and refractive index during agglomeration and surface growth. Proc Combust Inst 2019;37:1177–84. https://doi.org/10.1016/j.proci.2018.08.025.